THE JOURNAL OF PHYSICAL CHEMISTRY C

Article

pubs.acs.org/JPCC

Templated Synthesis and Chemical Behavior of Nickel Nanoparticles within High Aspect Ratio Silica Capsules

Nicholas C. Nelson, T. Purnima A. Ruberu, Malinda D. Reichert, and Javier Vela*

Department of Chemistry, Iowa State University, Ames, Iowa 50011, United States

ABSTRACT: One-dimensional transition metal nanostructures are of interest in many magnetic and catalytic applications. Using a combination of wet chemical synthesis, optical (infrared), and structural characterization methods (powder X-ray diffraction, scanning and transmission electron microscopy), we have investigated four paths to access 1D nickel nanostructures: (1) direct chemical reduction of a self-assembled nickel−hydrazine coordination complex, (2) thermal decomposition of the silica encapsulated nickel−hydrazine complex, (3) treatment of the silica encapsulated nickel−hydrazine complex with sodium borohydride followed by thermal annealing, and (4) electroless nickel plating using silica encapsulated nickel seed particles. We find that only route 1, which does not require a silica template, results in the formation of nickel nanorods, albeit some particle aggregation is observed. Routes 2 and 3 result in the formation of isotropic nickel structures under a reducing atmosphere. Route 4 results in heterogeneous nucleation and growth of existing particles only when partial etching of the silica capsule occurs. Detailed examination of the encapsulated nickel particles allows studying the effect of silica surface silanols on the oxidation of encapsulated nickel particles, the presence of nanoparticle−silica support interactions, the sintering mechanism of nickel and nickel oxide particles, and the fate of boride impurities. Nickel/silica nanostructures are strongly magnetic at room temperature.

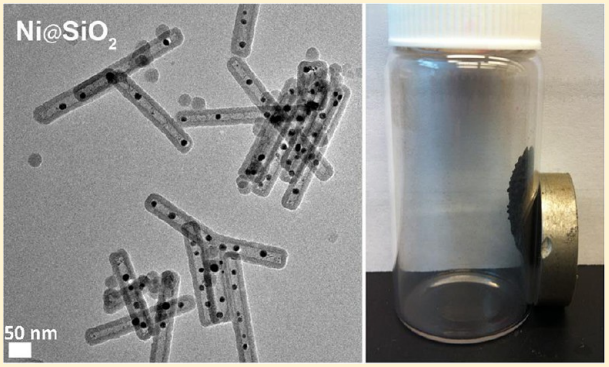

INTRODUCTION

Metallic and bimetallic nanostructures often possess unique chemical, magnetic, and/or optoelectronic properties. To cite one particular example, recent studies found that the kinetics of hydrogen sorption/desorption of light metal hydrides (magnesium) could be accelerated at near ambient temperature and pressure by introducing veins of a second, catalytic transition metal (iron, nickel, etc.).[1,2] Utilizing the known phenomenon of hydrogen spillover, these bimetallic heterostructures lower the activation energy required for reversible hydrogenation and dehydrogenation.[3,4] In view of this, we recently sought to fabricate one-dimensional (1D) nanostructures of first row transition metals such as nickel to further study similar behavior. Well-defined 1D nickel nanostructures could lead to new methods to synthesize other catalytic metals (Pd, Pt, Rh, Ru, Ir) via galvanic exchange.[5]

To date, 1D nickel nanostructures have been synthesized by colloidal and template methods. Among colloidal methods, Ni nanorods were made by reduction of $NiCl_2$ or $Ni(OH)_2$,[6,7] thermal decomposition of $Ni(CH_3COO)_2$, $Ni(COD)_2$ (COD = cycloocta-1,5-diene) or nickelocene,[8] solvothermal routes,[9−11] and the polyol process.[12,13] Among template methods, electrodeposition of nickel nanostructures using anodized or anodic aluminum oxide (AAO) has been heavily studied.[14,15] This technique has produced nickel nanowire arrays,[16−18] nickel nanotubes,[19,20] and nickel nanorods.[21−25] The resulting nickel nanorods exhibit superparamagnetic or soft ferromagnetic behavior depending on subsequent annealing conditions[26] and can be converted to nanoporous structures of other metals via galvanic exchange.[27] Nickel wires have also been made by electrodeposition into the nanochannels of glass templates.[28] Other commonly used templates include carbon nanotubes and polymers. Nickel nanowires were deposited in the interior of carbon nanotubes (CNTs) using electroless deposition.[29] Nickel nanorods were made inside multiwalled carbon nanotubes (MWCNTs) or carbon nanofibers using microwave plasma chemical vapor deposition (MPCVD)[30,31] or plasma-enhanced chemical vapor deposition (PECVD),[32] respectively. Arrays of ferromagnetic nickel nanowires[33] and nickel nanorods have been synthesized by electrochemical deposition using polycarbonate membranes.[34−36] Nickel nanorods were also prepared within the channels of block copolymers[37] or by annealing of dense composite films of NiO under H_2.[38] Unfortunately, these syntheses use expensive precursors and reagents and/or suffer from limited control over the final nanostructure morphology.

Catalytically active 1D nickel nanostructures have also been made using mesoporous silica templates, including SBA-15,[39,40] and two-dimensional (2D) mesoporous silica films.[41] Mesoporous silica templates are affordable and scalable. However, the presence of different pore lengths results in limited control over the aspect ratio of the new materials. For this reason, we

Received: October 4, 2013
Revised: November 14, 2013
Published: November 20, 2013

   dx.doi.org/10.1021/jp409878a | J. Phys. Chem. C 2013, 117, 25826−25836

turned our attention to the use of discrete, hollow 1D SiO_2 nanostructures as templates.[42−44] This class of templates can be subdivided into silica nanotubes and 1D silica capsules. The presence of openings at the tips of silica nanotubes complicates efforts to confine the growth of metals within their interior.[45−56] In contrast, silica nanocapsules offer a fully confined void against which new materials can be grown. Such silica nanocapsules can be synthesized by acid or basic catalyzed hydrolysis and condensation of tetraethyl orthosilicate (TEOS) or similar precursors in microemulsion using either soft (organic surfactants, DNA) or hard (coordination polymers) templates.[57−60]

Metal-based nanoparticles have indeed been synthesized within 1D silica nanocapsules. They include Fe/SiO_2 nanowires,[61] Fe_3O_4 nanoparticles,[62] Fe_3O_4−CdSe nanocomposites,[63] and Pd/SiO_2[60] and Ni/SiO_2 core/shells.[64−66] Ni@SiO_2 "yolk−shell" nanoreactors, prepared through direct silica coating followed by selective etching of the metal cores, are active catalysts for steam reforming of methane.[67] In this article, we present the results of a series of systematic attempts we made with the aim of confining the growth of 1D Ni(0) nanostructures within elongated silica capsules under a variety of conditions. Note: while this manuscript was in preparation, a report detailing a different, alternate synthesis of similar Ni⊂SiO_2 nanostructures (nickel particles encapsulated within silica capsules) appeared in the literature.[64]

EXPERIMENTAL SECTION

Materials. Brij 58 (poly(ethylene glycol) hexadecyl ether), tetraethyl orthosilicate (TEOS) (≥99.0%), borane−dimethylamine complex (97%), and gluconic acid ($C_6H_{12}O_7$) solution (50 wt % in H_2O) were purchased from Sigma-Aldrich; hydrazine monohydrate ($N_2H_4{\cdot}H_2O$) (100%, hydrazine 64%) and sodium borohydride (≥98%) from Acros; cyclohexane (99.9%), sodium hydroxide (99.4%), ammonium hydroxide (28.54%), diethylamine (reagent), and isopropanol (2-propanol) from Fisher; nickel(II) chloride hexahydrate (≥99.9% Ni) from Strem; nickel(II) acetate tetrahydrate (reagent) from J.T. Baker; and sodium tartrate dihydrate ($Na_2C_4H_4O_6{\cdot}2H_2O$) (97%) from Mallinckrodt. Hydrogen (99.995%) and argon (99.996%) were purchased from Linweld. All chemicals were used as received unless specified otherwise.

Synthesis. *$[Ni(N_2H_4)_3]Cl_2$⊂SiO_2* was prepared by a modified literature procedure. Briefly, Brij 58 (8.5 g, 7.6 mmol) was weighed into a 100 mL three-neck round-bottom (RB) flask equipped with a Teflon stir bar and a stainless steel thermocouple. The flask was purged with argon, cyclohexane (15 mL) was added, and the contents were heated to—and maintained at—50 °C in an oil bath. A 0.8 M $NiCl_2{\cdot}6H_2O$ aqueous solution (1.5 mL, 1.2 mmol) was added to the colorless solution and stirred until a transparent green reverse microemulsion formed. $N_2H_4{\cdot}H_2O$ (0.45 mL, 9.3 mmol) was added dropwise, causing a gradual color change to pink. After 3 h stirring, diethylamine (1.1 mL) was added, followed by TEOS (3.44 mL, 15.4 mmol). After 2 h stirring, the product was isolated by centrifugation (5000 rpm for 5 min), washed repeatedly with isopropanol, and dried in air at 60 °C for 12 h. *Treatment of $[Ni(N_2H_4)_3]Cl_2$⊂SiO_2 with $NaBH_4$.* $[Ni(N_2H_4)_3]Cl_2$⊂SiO_2 (1.2 g, ca. 1.2 mmol of Ni, assuming 100% conversion and recovery from the previous step above) was placed into a 125 mL flask equipped with a Teflon stir bar. H_2O (30 mL) was added and the suspension sonicated for 15 min. Freshly prepared 0.48 M $NaBH_4$ aqueous solution (5 mL, 2.4 mmol) was added dropwise while vigorously stirring the mixture at room temperature (RT), causing gas evolution and a color change to black. After 30 min stirring, the product was collected by centrifugation, washed with water and ethanol, and dried under vacuum for 6 h. The dry product (0.6 g) was placed into a ceramic combustion boat at the center of a 3 in. diameter quartz tube inside a three-zone Lindberg/Blue M tube furnace from Thermo Scientific. The tube was purged with a mixture of H_2 (10 mL/min) and Ar (50 mL/min) for 30 min, and the flow rates were maintained throughout the experiment. The tube was heated to 500 °C at 10 °C/min, maintained at 500 °C for 2 h, and then allowed to cool back to RT.

Electroless Nickel Plating Using N_2H_4. $Ni(CH_3COO)_2{\cdot}4H_2O$ (584 mg, 3.0 mmol) was dissolved in H_2O (25 mL). $Na_2C_4H_4O_6{\cdot}2H_2O$ (92.4 mg, 0.40 mmol), $C_6H_{12}O_7$ solution (1.48 g, 3.8 mmol), and $N_2H_4{\cdot}H_2O$ (0.49 mL, 10 mmol) were sequentially added. The pH was adjusted to 9.6 with NaOH. This solution was added to Ni⊂SiO_2 (35 mg), and the mixture heated to 75 °C in air, causing gas evolution. After 30 min stirring at 75 °C, the product was collected by centrifugation, washed several times with H_2O, and dried in air at 60 °C. *Using DMAB.* $Ni(CH_3COO)_2{\cdot}4H_2O$ (150 mg, 0.60 mmol) was dissolved in H_2O (20 mL). $C_6H_{12}O_7$ solution (1.32 g, 3.37 mmol) and DMAB (70.8 mg, 1.20 mmol) were sequentially added. The pH was adjusted to 6.8 with NH_4OH. This solution was added to Ni⊂SiO_2 (33 mg), and the mixture was heated to 45 °C in air, causing gas evolution. After 2.5 h stirring at 45 °C, the product was collected by centrifugation, washed several times with H_2O, and dried in air at 60 °C.

Characterization. *Powder X-ray diffraction* data were measured using Co Kα1, Kα2 split radiation (45 kV, 40 mA, λ_{avg} = 1.7903 Å) on a PANalytical X'Pert PRO diffractometer equipped with a theta−theta vertical mode goniometer, incident Fe filter, an air-cooled X'Celerator real time multiple strip (RTMS) detector, and spinner stage. The spectra were converted to Cu Kα radiation for comparison to standard patterns. Powder XRD data were also measured using Cu Kα1, Kα2 split radiation (45 kV, 40 mA, λ_{avg} = 1.5418 Å) on a PANalytical X'Pert PRO diffractometer equipped with a theta−theta vertical mode goniometer, diffracted beam Ni filter, an air-cooled X'Celerator RTMS detector, and spinner stage. Quantitative estimates of relative phase abundances (Ni vs NiO, and VT XRD, see below) were performed using Rietveld analysis on X'Pert HighScore Plus and GSAS software. The XRD samples were prepared by placing powders onto a background-less polycarbonate sample holder. *Transmission electron microscopy* was conducted using a FEI Technai G2 F20 field emission TEM and a scanning transmission electron microscope (STEM) operating at 200 kV (point-to-point resolution <0.25 nm and a line-to-line resolution of <0.10 nm). TEM samples were prepared by placing 2−3 drops of dilute ethanol suspensions onto carbon-coated copper grids. The composition of Ni⊂SiO_2 structures were characterized by energy dispersive spectroscopy (EDS) line scans in STEM mode. *Size and Morphology Analysis.* Particle dimensions were measured with ImageJ. In all cases, measurements and statistics were obtained for >50−100 $[Ni(N_2H_4)_3]Cl_2$ complexes, silica nanocapsules, or Ni^0 particles. Averages are reported ± standard deviations. *Scanning electron microscopy* was conducted using a FEI Quanta 250 FE-SEM (maximum resolution of 1.2 nm) equipped with secondary and backscattered electron detectors and IXRF Systems EDS system. SEM samples were prepared by placing 2−3 drops of dilute ethanol suspensions

dx.doi.org/10.1021/jp409878a | J. Phys. Chem. C 2013, 117, 25826−25836

onto glass coverslips. *Fourier transform infrared* spectra were recorded with a Bruker IFS66 V FT-IR spectrometer (transmittance mode) equipped with a DTGS detector with 16 scans at a resolution of 4 cm^{-1}. The samples were prepared by dilution with KBr and pressed into a pellet. Background spectra were collected under identical conditions. Samples were continuously purged with dry N_2 to minimize water vapor absorbance. *Ultraviolet–visible absorption* spectra were measured with a photodiode-array Agilent 8453 UV/vis spectrophotometer. Solvent absorption was recorded and subtracted from all spectra.

RESULTS AND DISCUSSION

Synthesis of 1D Ni(II)–Hydrazine Template and SiO_2 Capsules. Initial synthesis of $[Ni(N_2H_4)_3]Cl_2{\subset}SiO_2$ core–shell nanostructures was carried out in a water-in-oil reverse microemulsion by a slightly modified literature procedure.[68] Aqueous nickel(II) chloride hexahydrate ($NiCl_2{\cdot}6H_2O$) constituted the dispersed phase, cyclohexane was the continuous phase, and polyoxyethylene (20) cetyl ether (Brij58) was used as the surfactant. After mixing, a homogenized solution was obtained and hydrazine hydrate ($N_2H_4{\cdot}H_2O$) was added in excess. Under these conditions, a one-dimensional tris(hydrazine)nickel(II) chloride ($[Ni(N_2H_4)_3]Cl_2$) coordination polymer is formed. The 1D morphology of this material was confirmed by scanning electron microscopy (SEM), and the complex was identified by its characteristic, previously reported XRD pattern (Figure 1a,b). Template encapsulation by amorphous silica was achieved through *in situ* introduction of tetraethyl orthosilicate (TEOS), which easily undergoes hydrolysis and condensation in the presence of diethylamine to yield amorphous silica (Figure 1c,d). XRD clearly shows crystalline $[Ni(N_2H_4)_3]Cl_2$ is still present after coating.

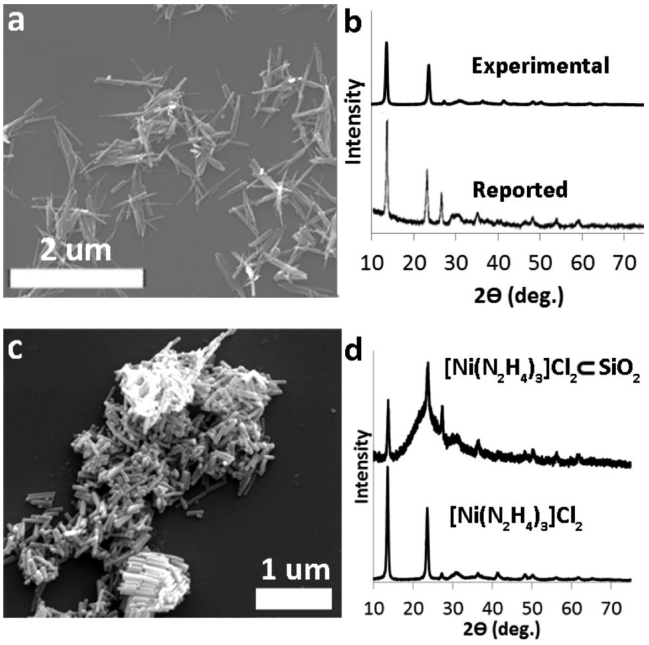

Figure 1. (a) SEM of $[Ni(N_2H_4)_3]Cl_2$ prepared by reverse microemulsion. (b) Experimental and reported XRD patterns for $[Ni(N_2H_4)_3]Cl_2$ template material.[69] (c) SEM of $[Ni(N_2H_4)_3]Cl_2{\subset}SiO_2$. (d) Experimental XRD pattern for $[Ni(N_2H_4)_3]Cl_2{\subset}SiO_2$ and reported XRD pattern for $[Ni(N_2H_4)_3]Cl_2$ (shown again for comparison).

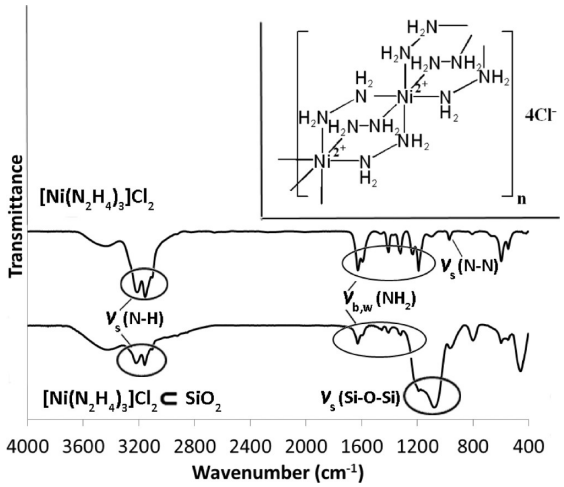

Figure 2. Experimental IR spectra of $[Ni(N_2H_4)_3]Cl_2$ and $[Ni(N_2H_4)_3]Cl_2{\subset}SiO_2$.[70] Inset shows possible Ni^{2+} coordination environment.

Infrared (IR) spectroscopy allows detecting the presence (or absence) of the N_2H_4 ligands and the SiO_2 shell (Figure 2). The N–H symmetric stretching vibrations at 3213 and 3156 cm^{-1} and the NH_2 bending and wagging vibrations between 1628 and 1192 cm^{-1} confirm the presence of hydrazine ligands in $[Ni(N_2H_4)_3]Cl_2$ and $[Ni(N_2H_4)_3]Cl_2{\subset}SiO_2$.[70] The N–N stretching frequency corroborates the bridging binding mode of the hydrazine ligands. N–N stretching frequencies for isomorphous $MCl_2(N_2H_4)_2$ (M = Mn, Fe, Co, Ni, Cu, Zn, Cd) complexes were previously identified using isotopic labeling and lie in the 960–985 cm^{-1} range.[71] A study of cobalt(II) complexes containing monodentate $[Co(N_2H_4)_6]Cl_2$ (ν(N–N) = 928 cm^{-1}) or bidentate hydrazine $[Co(N_2H_4)_2]Cl_2$ (ν(N–N) = 970 cm^{-1}) confirmed that the N–N stretching frequency is more blue-shifted for the latter, more rigid, bidentate coordination mode.[72] Experimental $[Ni(N_2H_4)_3]Cl_2$ spectra clearly show a peak at 972 cm^{-1} and can be similarly attributed to N–N stretching. A possible coordination environment consistent with the above information is shown as an inset of Figure 2. The IR spectrum of $[Ni(N_2H_4)_3]Cl_2{\subset}SiO_2$ shows a strong, broad peak at 1190–1090 cm^{-1} that can be attributed to the longitudinal- (LO) and transverse-optical (TO) components of the asymmetric Si–O–Si bond stretching vibration.[73] The bands at 801 and 461 cm^{-1} correspond to Si–O–Si symmetric stretching and bending vibrations, respectively.[73]

As observed previously, treatment of $[Ni(N_2H_4)_3]Cl_2{\subset}SiO_2$ with hydrochloric acid (HCl) results in complete etching of the tris(hydrazine)nickel(II) chloride core, while the amorphous 1D silica shell is retained.[68] TEM confirms these silica templates have an elongated, nanocapsule morphology (Figure 3a). The thickness of the silica walls depends on the amount of TEOS used as well as the time used for hydrolysis and condensation reactions. Typical wall thicknesses are 15–20 nm under the conditions and times used here. IR spectroscopy confirms the hydrazine ligands are no longer present after acid etching, as evidenced by the lack of bands at 3213 and 3156 cm^{-1} (Figure 3b). The peaks at 2849 and 2919 cm^{-1} characteristic of C–H stretching could be attributed to incomplete removal of Brij 58 surfactant. XRD confirms removal of the original crystalline core (Figure 3c). As reported, different initial concentrations of aqueous $NiCl_2{\cdot}6H_2O$ while

dx.doi.org/10.1021/jp409878a | J. Phys. Chem. C 2013, 117, 25826–25836

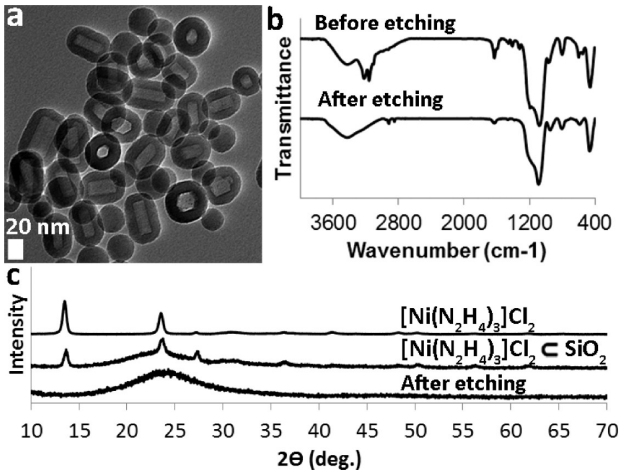

Figure 3. (a) TEM of void silica nanocapsules after HCl etching. (b) IR spectra before and after HCl etching. (c) Experimental XRD patterns of $[Ni(N_2H_4)_3]Cl_2$, $[Ni(N_2H_4)_3]Cl_2{\subset}SiO_2$, and HCl-etched silica nanocapsules.

keeping the amount of Brij 58 and hydrazine constant allows the isolation of nanocapsules with different lengths (Figure 4a–e).[68] The overall width (outer diameter) of the nanocapsules in all experiments (40–70 nm) is constant and depends on the length of the surfactant polyoxyethylene chain used.[68]

Trying To Access Zerovalent Nickel by Different Routes: Direct Reduction of $[Ni(N_2H_4)_3]Cl_2$. Following our initial idea of trying to synthesize zerovalent Ni(0) nanorods, we actually first explored the direct chemical reduction of surfactant-stabilized tris(hydrazine)nickel(II) chloride (i.e., in the absence of the SiO_2 shell). Hydrazine is a powerful reducing agent when present in alkaline (basic) environments and is capable of reducing Ni^{2+} (Scheme 1).[69] Reduction of

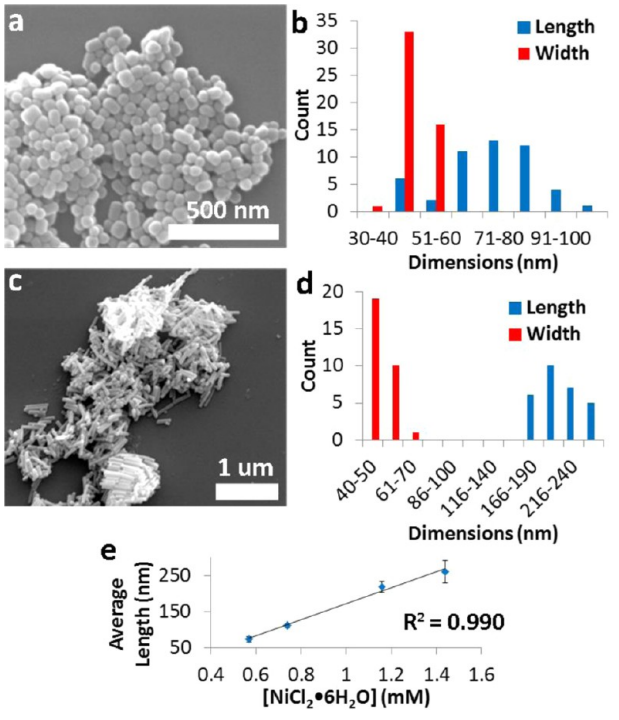

Figure 4. (a, c) SEM micrographs and (b, d) corresponding size histograms of silica nanocapsules prepared with different initial concentrations of $NiCl_2$. (e) Plot of silica nanocapsule length versus initial nickel concentration.

Scheme 1

(a) $N_2H_4 + 4^-OH \longrightarrow N_2 + 4H_2O + 4e^-$ $E^\circ = -1.16$ V

(b) $Ni^{2+} + 2e^- \longrightarrow Ni^0$ $E^\circ = -0.76$ V

$[Ni(N_2H_4)_3]Cl_2$ complex by introduction of hydroxide (^-OH) ions has been used in the synthesis of nickel powders.[69] Given the 1D morphology of the $[Ni(N_2H_4)_3]Cl_2$ complex formed by reverse microemulsion (above), we explored whether the introduction of hydroxide ion could directly result in reduction while maintaining morphology. Previous XRD studies suggest that reduction of $[Ni(N_2H_4)_3]Cl_2$ complex by addition of hydroxide ion proceeds through a nickel hydroxide ($Ni(OH)_2$) intermediate.[69] In our case, *in situ* addition of sodium hydroxide (NaOH) to freshly formed $[Ni(N_2H_4)_3]Cl_2$ complex resulted in face-centered cubic nickel (fcc-Ni^0), as confirmed by XRD (Figure 5a). However, TEM shows the

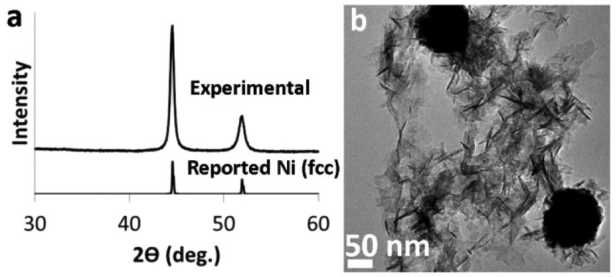

Figure 5. (a) XRD and (b) TEM of partially aggregated fcc-Ni nanorods obtained from *in situ* addition of NaOH to self-assembled 1D $[Ni(N_2H_4)_3]Cl_2$ in reverse microemulsion.

product consists of a mixture of Ni particles, some of which have the desired elongated (1D) morphology and some of which are significantly aggregated (forming spheroidal clumps) (Figure 5b). Better control over the addition rate of NaOH, or additional surfactants, may allow obtaining the desired 1D Ni^0 morphology.

Thermal Decomposition of $[Ni(N_2H_4)_3]Cl_2{\subset}SiO_2$. The next approach we tried to synthesize Ni^0 nanorods was to decompose $[Ni(N_2H_4)_3]Cl_2{\subset}SiO_2$ (within the capsules) by heating to 500 °C (at a 10 °C min^{-1} rate) under either Ar or Ar/H_2 atmosphere. TEM shows heating under Ar results in 1D material filling the interior of the nanocapsules (Figure 6a,b). However, after the reaction there is a significant amount of void capsules (ca. 75%), suggesting that a mobile Ni species diffused away during heating. In addition, XRD shows the presence of both desired fcc-Ni^0 and undesired rock salt NiO, with the latter being the major phase. To circumvent the formation of NiO, the reaction was carried out under an Ar/H_2 reducing environment. In this case, XRD shows the major product is fcc-Ni^0. Unfortunately, in this case TEM shows the absence of any 1D nickel and a larger fraction of void capsules (ca. 77%) (Figure 6c,d).

Where Did Nickel Go? Thermal treatment of metal–hydrazine complexes $[M(N_2H_4)_n]^{2+}$ (M = Mn(II), Fe(II), Co(II), Ni(II), Zn(II), and Cd(II), n = 2 or 3) can result in loss of hydrazine followed by metal oxide formation.[74] Hydrazine itself undergoes thermal decomposition to N_2 and NH_3 at 240

dx.doi.org/10.1021/jp409878a | J. Phys. Chem. C 2013, 117, 25826–25836

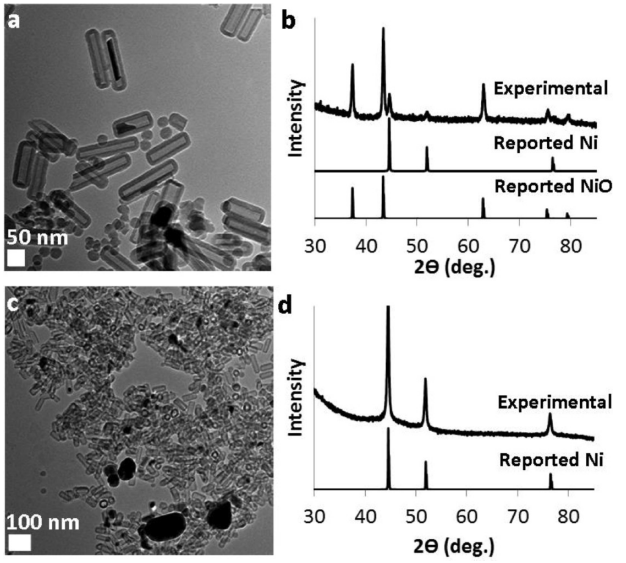

Figure 6. (a) TEM and (b) XRD of $[Ni(N_2H_4)_3]Cl_2{\subset}SiO_2$ after heating under Ar. (c) TEM and (d) XRD of $[Ni(N_2H_4)_3]Cl_2{\subset}SiO_2$ after heating under Ar/H_2.

°C.[75] Gaseous byproducts from hydrazine decomposition during thermal decomposition of $[Ni(N_2H_4)_3]Cl_2{\subset}SiO_2$ under Ar/H_2 could explain why many capsules prepared in this way are void of Ni metal. Previous studies on heat treatment of nickel particles on metal oxide surfaces showed that NH_3 and H_2 environments lead to substantially higher particle mobility and increased sintering rates.[76] Ammonia produced by hydrazine decomposition coupled with the hydrogen reducing environment could lead to formation of mobile species that give rise to the observed diffusion and agglomeration of nickel outside of the nanocapsules (Figure 6c). A similar argument could be made for thermal decomposition under Ar, whereby the newly formed Ni^0 particles could act as a catalyst for the decomposition of NH_3 (from hydrazine ligand) to N_2 and H_2, thereby producing a NH_3/H_2 environment.

Reduction with $NaBH_4$. The next approach we tried to obtain 1D Ni^0 was to chemically reduce $[Ni(N_2H_4)_3]Cl_2{\subset}SiO_2$ (encapsulated) suspended in H_2O by slow addition of $NaBH_4$. The suspension immediately underwent a color change from pink to black and copious amounts of gas evolved. The IR spectrum (Figure 7a) of the product confirms hydrazine ligands are no longer present, and XRD (Figure 7b) shows the absence of crystalline material. TEM (Figure 6c) shows varying degrees of contrast along the length of the nanocapsule, suggesting there is still some (Ni) material within the SiO_2 cavity. Reacting aqueous nickel salts with sodium borohydride is known to yield amorphous nickel/nickel boride (Ni^0/Ni_xB_y) products[77−79] (Scheme 2a−c), although the mechanism by which Ni_xB_y forms remains unknown.[80] The stoichiometry of the final compound (values of "*x*" and "*y*") obtained upon crystallization depends on the amount of boron in the amorphous material. Crystallization of Ni^0/Ni_xB_y is often achieved through thermal annealing at ca. 500 °C under an inert atmosphere, and XRD analysis has shown fcc-Ni tends to be the major product.[81] However, when we thermally annealed the $NaBH_4$ treated material, we obtained rock salt nickel oxide (NiO) as the prevalent phase (Figure 8). An average crystallite size of 5.3 nm was found using the Scherrer equation. TEM (Figure 8) shows

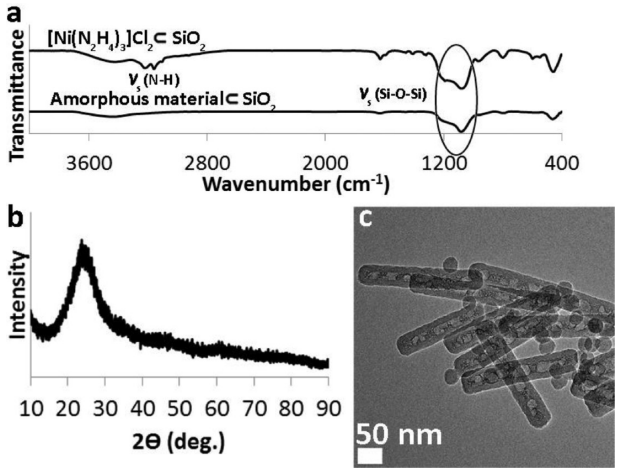

Figure 7. (a) IR, (b) XRD, and (c) TEM of $[Ni(N_2H_4)_3]Cl_2{\subset}SiO_2$ after treatment with NaBH4.

Scheme 2

(a) $BH_4^- + 4H_2O \longrightarrow B(OH)_4^- + 4H^+ + 2H_2 + 4e^-$

(b) $2Ni^{2+} + 4e^- \longrightarrow 2Ni^0$

(c) $2Ni^{2+} + BH_4^- + 4H_2O \longrightarrow 2Ni^0 + B(OH)_4^- + 4H^+ + 2H_2$

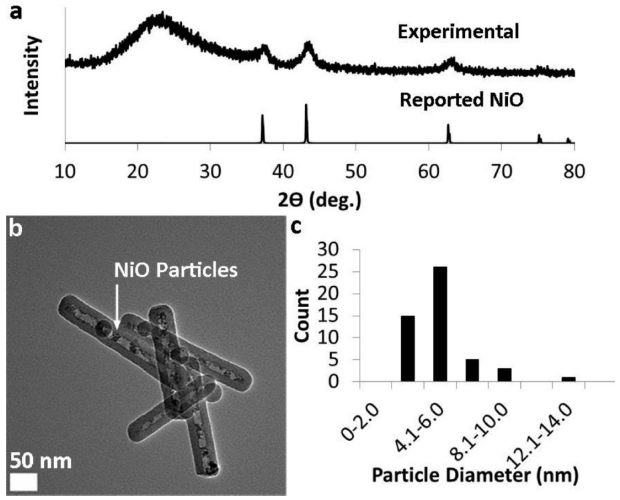

Figure 8. (a) XRD, (b) TEM, and (c) particle size histogram for $NiO{\subset}SiO_2$ obtained after thermal annealing (500 °C/Ar) of $NaBH_4$-treated $[Ni(N_2H_4)_3]Cl_2{\subset}SiO_2$.

an average particle size (4.9 ± 2.0 nm) that is in good agreement with the XRD value.

Where Did the Oxide Come From? The Role of Silanol Groups. $NiO{\subset}SiO_2$ formed under an Ar atmosphere, in the absence of an obvious O_2 or H_2O source. We thus wondered what was the source of oxygen in this reaction. Silanol (Si−OH) groups are known to undergo dehydration at elevated temperatures, and we thought this might be the source of oxygen giving rise to $NiO{\subset}SiO_2$.[82] Silanol dehydration upon heating was confirmed by comparing the IR spectra of as-synthesized and calcined silicas (*as*-SiO_2 and *c*-SiO_2, respectively) (Figure 9a). The IR spectra clearly show the Si−OH stretching frequency at 947 cm^{-1} is present in *as*-SiO_2,

dx.doi.org/10.1021/jp409878a | J. Phys. Chem. C 2013, 117, 25826−25836

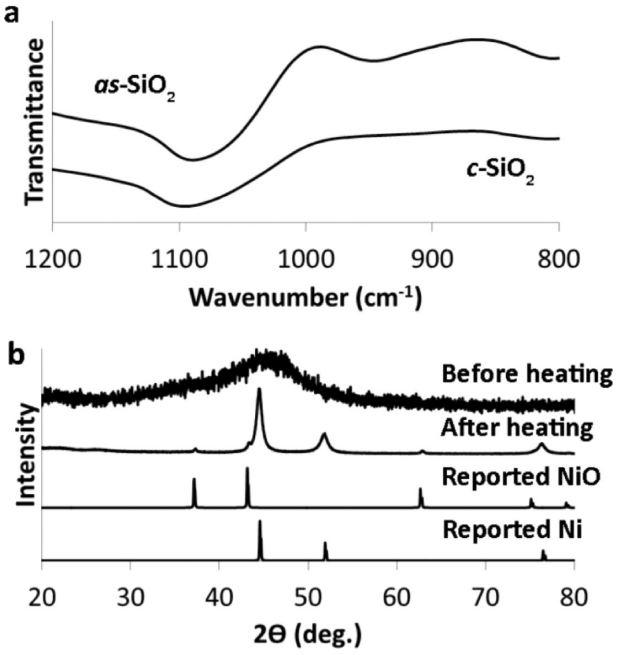

Figure 9. (a) IR spectrum showing dehydration of Si−OH groups (loss of 947 cm^{-1} peak) in SiO_2 capsules upon calcination. (b) XRD pattern of $NaBH_4$-treated $[Ni(N_2H_4)_3]Cl_2$ (in the absence of SiO_2 capsule) and its calcination product (mostly Ni). Reported XRD patterns for rock salt NiO and fcc-Ni are shown for comparison.

but upon calcination at 500 °C the Si−OH stretching frequency is no longer present in *c*-SiO_2. To test this idea, the heating procedure above was repeated without the silica shell. An aqueous suspension of polymeric $[Ni(N_2H_4)_3]Cl_2$ (see above) was treated with $NaBH_4$, and the resulting as-synthesized material was calcined under Ar flow at 500 °C at a heating rate of 10 °C min^{-1}. Indeed, calcination in this case resulted in nearly phase pure fcc-Ni as shown by XRD (Figure 9b). The XRD also shows a minor rock salt NiO component that could have formed from trace O_2 or H_2O originally present in the tube. However, X'Pert HighScore Plus structural refinement shows the product in this case consists of about 95% Ni and 5% NiO.

In order to circumvent nickel oxidation in the presence of silica during calcination of $[Ni(N_2H_4)_3]Cl_2$⊂SiO_2, the same thermal reaction was rerun under the flow of a reducing, Ar/H_2 mixture while keeping all other conditions identical. In this case, the XRD pattern of the product (Figure 10) shows fcc-Ni^0 with an average crystallite size of 12 nm estimated using the Scherrer equation. This appears to be in good agreement with the average particle size (13.7 ± 3.5 nm) obtained for the larger of two different populations of Ni particles observed by TEM (Figure 10f). The average number of particles per rod is 4 ± 2 (Figure 10g). Only about 1% of the capsules were void of particles. EDX line scans were used to confirm that the high contrast particles within the SiO_2 cavity are rich in Ni (Figure 10e). Fast fourier transform of selected area electron diffraction (SAED) under HR TEM yielded *d*-spacings corresponding to (111) and (200) planes of fcc-Ni (Figure 10c). Also observed where (111) and (200) planes from rock salt NiO, which can be attributed to a thin surface layer of oxide present coating the Ni particles. This thin oxide layer may help passivate and protect Ni, making Ni more stable toward further oxidation at ambient temperature and pressure.

In contrast to the initial $[Ni(N_2H_4)_3]Cl_2$⊂SiO_2 materials, $NaBH_4$ treatment results in the loss of a significant amount of the original fill volume of the nanocapsule in the form of N_2H_4, as confirmed by IR analysis (above). We believe this volume loss explains why nanorods are not formed during the subsequent calcination step: After hydrazine loss, there is simply not enough Ni^0 to entirely fill the nanocapsule cavity. Nevertheless, the resulting Ni⊂SiO_2 heterostructures display strong (ferro)magnetic behavior at room temperature (Figure 11). Other magnetic 1D metals coated with silica are known.[61−63,66,83]

Following the above $NaBH_4$/calcination procedure, we were able to modify the final Ni^0 particle size by simply varying the amount of aqueous $NiCl_2$ used during the original synthesis of the SiO_2 capsules. In this way, the [Brij 58]:[$NiCl_2$] ratio was held constant at 5:1, and different amounts of aqueous $NiCl_2$ were added. As shown in Figure 12, increasing the $NiCl_2$ loading results in larger final Ni average particle sizes and in a small decrease in the average number of Ni particles per capsule. A recent literature report found a similar correlation.[64] In conventional Ni/SiO_2 particles for catalysis, Ni^0 particle size is proportional to Ni(II) precursor loading.[84]

Nanoparticle−Support Interactions and Sintering Mechanism. It is interesting to note that calcination of $NaBH_4$-treated $[Ni(N_2H_4)_3]Cl_2$⊂SiO_2 under Ar/H_2 appears to yield some larger fcc-Ni particles (up to 17−21 nm), whereas

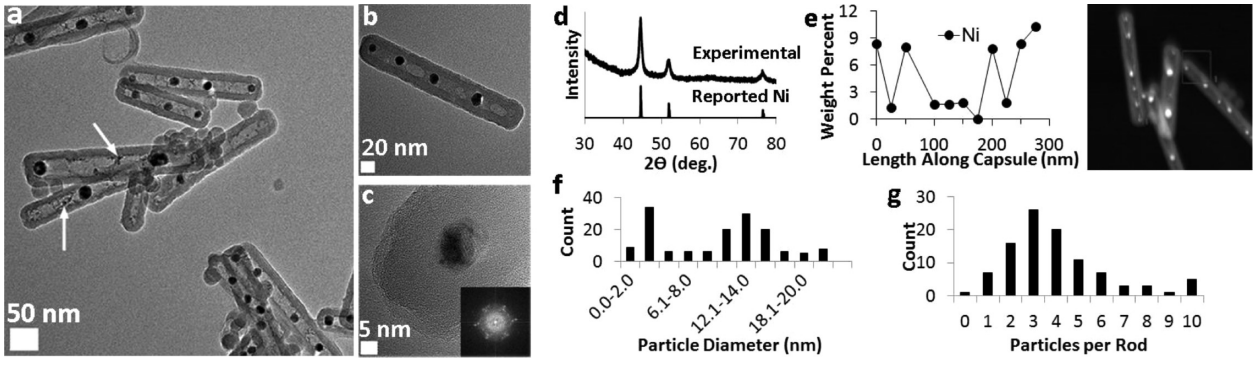

Figure 10. (a, b) TEM and (c) HRTEM micrographs and corresponding SAED (inset) for Ni⊂SiO_2. (d) Experimental XRD pattern for Ni⊂SiO_2 (top) and reported XRD pattern for Ni (bottom). (e) Plot of weight percent nickel along the length a SiO_2 capsule from EDX/dark field TEM (scan direction is top to bottom). (f) Bimodal Ni particle size distribution in Ni⊂SiO_2 obtained by calcination under an Ar/H_2 atmosphere. (g) Histogram showing number of Ni particles per SiO_2 capsule.

dx.doi.org/10.1021/jp409878a | J. Phys. Chem. C 2013, 117, 25826−25836

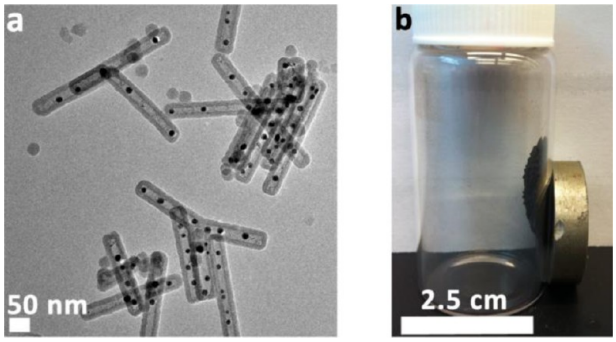

Figure 11. (a) Another representative TEM micrograph of Ni⊂SiO_2 heterostructures. (b) Photograph showing their strongly magnetic behavior.

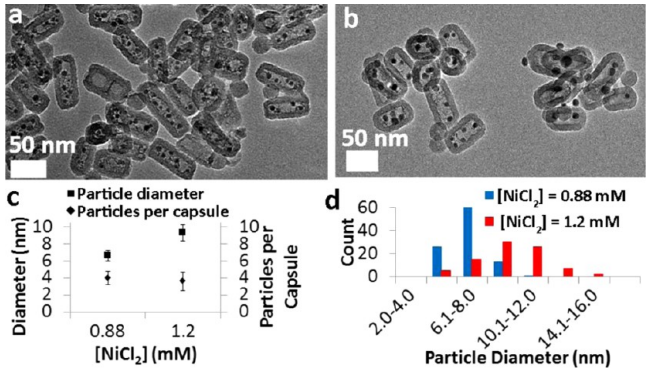

Figure 12. (a) TEM micrograph of Ni⊂SiO_2 using 0.88 mM $NiCl_2$. (b) TEM micrograph of Ni⊂SiO_2 using 1.2 mM $NiCl_2$. (c) Plot of particles per capsule and diameter vs [$NiCl_2$]. (d) Plot of average nanocapsule cavity dimensions vs [$NiCl_2$].

calcination under Ar resulted in relatively smaller NiO particles sizes (up to 6−8 nm) (Figures 10 and 8, respectively). This observation may be explained by particle−support interactions: Nickel oxides interact more strongly with oxide supports than nickel metal, thus resulting in less particle mobility, lower sintering rates, and therefore smaller particle sizes (for NiO⊂SiO_2).[85] TEM also shows the NiO particles are more thoroughly spread on the surface of the silica cavity compared to Ni^0 particles, likely to the increased particle−support interactions (Figure 8a).

In addition, calcination of $NaBH_4$-treated $[Ni(N_2H_4)_3]Cl_2$⊂SiO_2 under Ar/H_2 resulted in spherically shaped fcc-Ni^0 particles, whereas calcination under Ar resulted in NiO particles that exhibit comparatively less shape uniformity (Figures 10f and 8c, respectively). This suggests that during the decomposition of $NaBH_4$-treated $[Ni(N_2H_4)_3]Cl_2$⊂SiO_2 the resulting Ni^0 particles are able to sinter at higher rates relative to NiO particles, leading to the observed more regular, spherical morphology. Two mechanisms used to explain sintering in supported Ni^0 particles are atomic migration (Ostwald ripening) and particle migration (coalescence). The mechanism of Ni^0 sintering on silica depends on the atmosphere used during calcination.[86,87] Ni^0 particle sintering has been shown to occur through both mechanisms under vacuum. However, under a reducing (H_2) atmosphere, particle migration is suppressed and atomic migration becomes the predominant mechanism attributed to increased interaction between the Ni^0 particle and the silica support, relative to vacuum. At high magnification, TEM actually shows a secondary population of very small ca. 2−4 nm particles in the Ni⊂SiO_2 sample (Figure 10f); this indicates a bimodal size distribution and is consistent with an atomic migration sintering mechanism. However, other factors such as support porosity and surface impurities may also play a role in the formation of spherical nickel particles.[85]

Examining the Fate of Boron. As mentioned above, the reaction between $[Ni(N_2H_4)_3]Cl_2$ and $NaBH_4$ initially yields an unidentified, noncrystalline product, a fraction of which could be amorphous nickel borides (Ni_xB_y). To probe the possible presence (and speciation) of boron in these samples, a sample made by treating $[Ni(N_2H_4)_3]Cl_2$ with $NaBH_4$ was studied by variable temperature (hot-stage) VT XRD. Upon heating, this experiment clearly shows the as-obtained amorphous material undergoing structural organization to yield fcc-Ni (Figure 13).

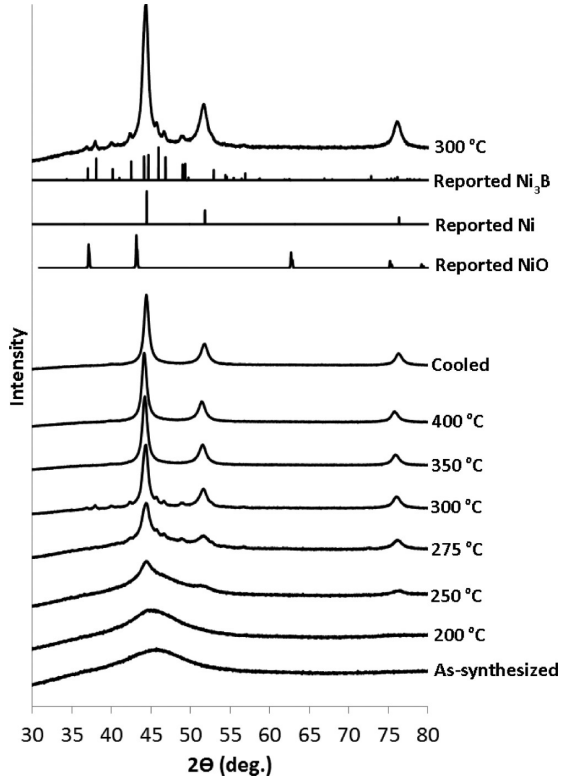

Figure 13. VT XRD data obtained for $NaBH_4$-treated $[Ni(N_2H_4)_3]Cl$ (heating rate 5 °C min^{-1}). Reported XRD patterns for orthorhombic Ni_3B, fcc-Ni, and rock salt NiO, as well as the 300 °C XRD pattern (repeated), are shown at the top for comparison and easy reference.

In addition, the diffraction pattern at 275 °C shows the emergence of an extra set of peaks not attributable to fcc-Ni. These peaks become even more pronounced at 300 °C and eventually disappear at 350 °C. The extra peaks observed in the diffraction pattern obtained at 300 °C match well with the reported XRD pattern of orthorhombic nickel boride (Ni_3B) (Figure 13). General Structure Analysis System[88] (GSAS) structural refinement shows the crystalline material obtained at 300 °C consists of about 91% Ni and 9% Ni_3B. A slight observed shift to lower 2θ angle relative to the standard pattern may be due to thermal expansion of the lattice at the temperature used to collect the XRD. The shift to lower 2θ values is also demonstrated by observing the XRD patterns at 350 and 400 °C compared to the fcc-Ni standard pattern and the XRD pattern of the calcined product at 35 °C (Figure 13). Any Ni_3B phase has completely decomposed at 400 °C, but the

dx.doi.org/10.1021/jp409878a | J. Phys. Chem. C 2013, 117, 25826−25836

decomposition product is unknown. Previous XPS analyses on amorphous Ni−B materials suggest possible dismutation to boron trioxide (B_2O_3) and Ni_xB_y.[81,89,90] It is unlikely the intermediate Ni_3B phase undergoes gaseous decomposition due to its high boiling point but transforms instead to an amorphous form a stable boron oxide (B_2O_3). B_2O_3 is difficult to crystallize at STP and could be why this phase is not detected by XRD.[91] Further elemental analysis and XPS studies may be necessary to fully establish the fate of the Ni_3B phase.

Electroless Ni Plating: Heterogeneous Growth vs Homogeneous Nucleation. The final approach we explored to try to grow zerovalent nickel nanorods within 1D silica capsules was to use the metal particles within Ni⊂SiO_2 as seeds for heterogeneous nucleation. To test this idea, we used electroless nickel plating.[80] Electroless plating is characterized by the selective reduction of aqueous metal ions at the surface of a catalytically active substrate (e.g., Ni, Fe, Co, Rh, Pd, Pt). This catalyzed (seeded) process has been used in the deposition of nickel metal, nickel phosphide, or nickel boride depending on the reducing agent employed.[78,92,93] Reducing agents and conditions commonly employed in electroless nickel plating include sodium borohydride at high temperature, hydrazine under basic (alkaline) conditions, and dimethylamineborane.[80] Electroless nickel plating in alkaline N_2H_4 solution results in a minor growth of the fcc-Ni within the capsules. The average crystallite size calculated from XRD using the Scherrer equation suggests an increase from 9.1 to 10.9 nm, albeit TEM micrographs show a statistically insignificant increase from 13.6 ± 2.8 to 16.1 ± 4.6 nm (Figure 14). In addition, free Ni^0 particles are also found outside of the silica capsules (Figure 14). This could result from homogeneous nucleation and/or from silica etching under the basic conditions used. The presence of several "thinner" and some ruptured silica capsules provides evidence for etching (Figure 14).

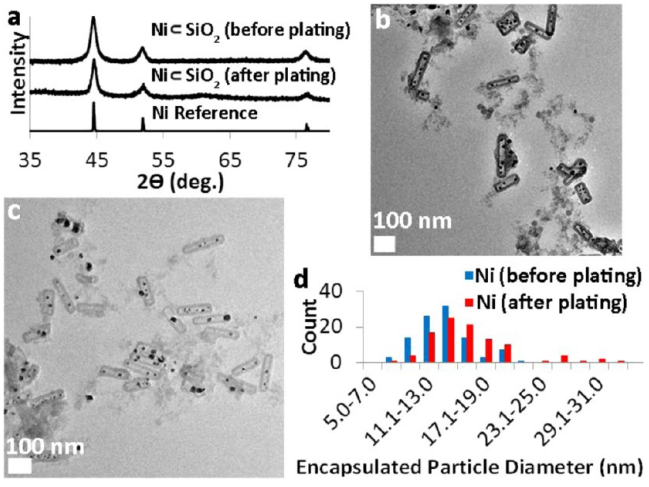

Figure 14. (a) XRD pattern of Ni⊂SiO_2 before and after plating. (b, c) TEM micrographs of Ni⊂SiO_2 after plating. (d) Particle size distribution histogram of encapsulated Ni particles.

Electroless nickel-plating with dimethylamineborane (DMAB) resulted in the formation of some new amorphous material and in homogeneous nucleation of new fcc-Ni particles, as evidenced by XRD (Figure 15). High temperature annealing of these products under an Ar/H_2 atmosphere resulted in a cleaner powder diffraction pattern indicative of a larger fcc-Ni particle size as evidenced by a decrease in XRD peak widths. However, TEM shows no growth occurred within the nanocapsules (8.6 ± 1.9 and 8.6 ± 1.3 nm before and after annealing, respectively) (Figure 16b,c). Further, agglomerated material was observed outside of the nanocapsules (Figure 16c), which strongly suggests homogeneous nucleation occurred.

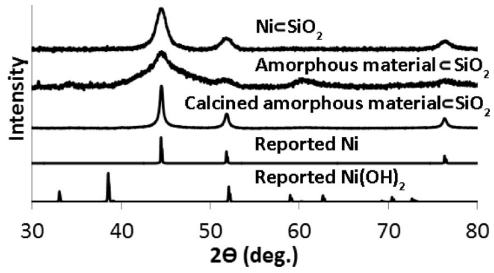

Figure 15. XRD patterns or electroless nickel plating using DMAB as reductant.

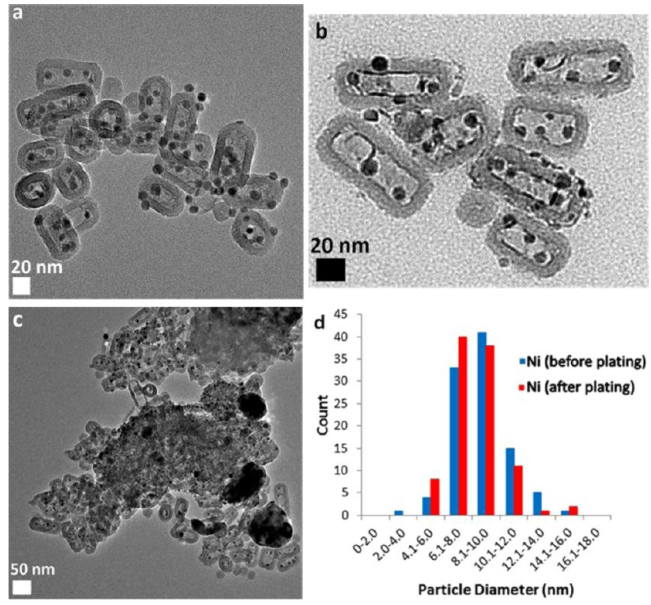

Figure 16. (a) TEM micrograph of Ni⊂SiO_2 before plating. (b, c) TEM micrographs of Ni⊂SiO_2 after plating. (d) Particle size distribution histogram for Ni⊂SiO_2 before and after plating using DMAB as reducing agent.

Thus, while conditions used for electroless nickel plating with N_2H_4 etch silica, conditions used for electroless nickel plating using DMAB result in homogeneous nucleation of new nickel particles. The fact that using DMAB under neutral pH did not lead to particle growth strongly suggests that the calcined silica shell may not be sufficiently porous to permit the transport of nickel(II) precursor and reductant from the outer solution and onto the surface of the Ni(0) seeds within the nanocapsule cavity. It may be possible to decrease the density of the silica shell through co-condensation of TEOS with an alkyl-functionalized silane, followed by calcination to remove the organic component or by chemical etching in alkaline solution. However, this is out of the scope of the present work and will have to be addressed in the future.

dx.doi.org/10.1021/jp409878a | J. Phys. Chem. C 2013, 117, 25826−25836

CONCLUSIONS

One-dimensional nanostructures of catalytic transition metals such as nickel are of interest in many applications, for example in interpenetrated, bimetallic hydrogen storage materials. In this paper, we have explored the use of elongated silica capsules to template the growth of such 1D nickel(0) nanostructures (Scheme 3). We find that morphology considerations aside, zerovalent nickel (fcc) particles can be accessed by (1) direct chemical reduction of a self-assembled $[Ni(N_2H_4)_3]Cl_2$ coordination complex in the absence of SiO_2 capsules, (2) thermal decomposition of $[Ni(N_2H_4)_3]Cl_2{\subset}SiO_2$ under a reducing H_2/Ar atmosphere, and (3) thermal annealing of $NaBH_4$-treated of $[Ni(N_2H_4)_3]Cl_2{\subset}SiO_2$ under a reducing H_2/Ar atmosphere.

Scheme 3

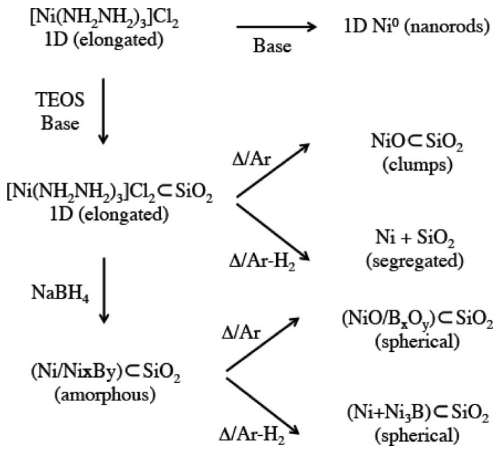

Among these three routes, only (1) results in the formation of 1D Ni(0) nanostructures, albeit particle aggregation will need to be suppressed, perhaps by adding extra surfactants to passivate the surface of the newly formed metal particles. Interestingly, route 1 does not require a silica template. Routes 2 and 3 both result in the formation of more isotropic Ni(0) structures, without an apparent 1D fraction. In the absence of a reducing atmosphere (H_2 gas), silanols on the surface of the silica capsules generate water vapor that lead to metal oxidation. This results in the formation of NiO (rock salt) nanostructures, some of which are elongated (route 2). An examination of Ni vs NiO particle sizes and distributions per capsule may help explain how these materials interact with the silica support as well as their sintering mechanism. Route 3 can reliably generate silica capsules containing several spheroidal Ni(0) particles within their cavities. These peapod-like $Ni{\subset}SiO_2$ heterostructures display strong magnetic behavior at room temperature, and preliminary data suggest Ni(0) particle size can be tuned while maintaining the overall capsule dimensions. Variable temperature experiments designed to probe the fate of boron, originating from $NaBH_4$ reductant used in (3), revealed the presence of amorphous boride impurities, which crystallize Ni_3B upon further annealing.

We also attempted to grow one-dimensional nickel nanostructures via (4) electroless Ni plating using $Ni{\subset}SiO_2$ as seeds. Discernible heterogeneous nucleation and growth on the encapsulated Ni(0) particles was observed using N_2H_4 as the reductant; however, the silica shell was etched during growth due to basic conditions employed. Experiments conducted at neutral pH using DMAB as the reductant resulted in no internal growth of encapsulated Ni(0) particles. Future work will be necessary in order to determine what are the best conditions required to effectively produce 1D nanostructures within silica nanocapsules or other similar templates.

AUTHOR INFORMATION

Corresponding Author

*Phone 515-294-5536; e-mail vela@iastate.edu.

Notes

The authors declare no competing financial interest.

ACKNOWLEDGMENTS

J.V. thanks Iowa State University for startup funds. The authors thank Matt Besser for assistance with structural characterization. *Disclosure:* this article is the result of experimental work (2010−2012) conducted as part of a MS thesis (N.C.N.). During production of this manuscript, a related (but not identical) article appeared.[64] This and the present manuscript complement each other and will together help better understand $Ni{\subset}SiO_2$ and other similarly heterostructured nanomaterials.

REFERENCES

(1) Bérubé, V.; Radtke, G.; Dresselhaus, M.; Chen, G. Size Effects on the Hydrogen Storage Properties of Nanostructured Metal Hydrides: A Review. *Int. J. Energy Res.* **2007**, *31*, 637−663.

(2) Tan, Z. P.; Chiu, C.; Heilweil, E. J.; Bendersky, L. A. Thermodynamics, Kinetics and Microstructural Evolution during Hydrogenation of Iron-Doped Magnesium Thin Films. *Int. J. Hydrogen Energy* **2011**, *36*, 9702−9713.

(3) Bogdanovic, B.; Sandrock, G. Catalyzed Complex Metal Hydrides. *MRS Bull.* **2002**, *27*, 712−716.

(4) Bogdanovic, B.; Schwickardi, M. Ti-Doped Alkali Metal Aluminium Hydrides as Potential Novel Reversible Hydrogen Storage Materials. *J. Alloys Compd.* **1997**, *253*, 1−9.

(5) González, E.; Arbiol, J.; Puntes, V. F. Carving at the Nanoscale: Sequential Galvanic Exchange and Kirkendall Growth at Room Temperature. *Science* **2011**, *334*, 1377−1380.

(6) Luo, Y.; Zhang, J.-C.; Shen, Y.; Jiang, S.-T.; Liu, G.-Y.; Wang, L-J. T. Preparation and Magnetic Properties of Nickel Nanorods by Thermal Decomposition Reducing Methods. *Trans. Nonferrous Met. Soc. China* **2006**, *16*, s96−s100.

(7) Ni, X.; Su, X.; Yang, Z.; Zheng, H. The Preparation of Nickel Nanorods in Water-in-Oil Microemulsion. *J. Cryst. Growth* **2003**, *252*, 612−617.

(8) Cordente, N.; Respaud, M.; Senocq, F.; Casanove, M.; Amiens, C.; Chaudret, B. Synthesis and Magnetic Properties of Nickel Nanorods. *Nano Lett.* **2001**, *1*, 565−568.

(9) Ghosh, S.; Ghosh, M.; Rao, C. N. R. Nanocrystals, Nanorods and Other Nanostructures of Nickel, Ruthenium, Rhodium and Iridium Prepared by a Simple Solvothermal Procedure. *J. Cluster Sci.* **2006**, *18*, 97−111.

(10) Alagiri, M.; Muthamizhchelvan, C.; Ponnusamy, S. Solvothermal Synthesis of Nickel Nanorods and Its Magnetic, Structural and Surface Morphological Behavior. *Mater. Lett.* **2011**, *65*, 1565−1568.

(11) Guo, Y.; Wang, G.; Wang, Y.; Huang, Y.; Wang, F. Large-Scale and Shape-Controlled Synthesis and Characterization of Nanorod-Like Nickel Powders Under Microwave Radiation. *Mater. Res. Bull.* **2012**, *47*, 6−11.

(12) Yu, K.; Kim, D. J.; Chung, H. S.; Liang, H. Dispersed Rodlike Nickel Powder Synthesized by Modified Polyol Process. *Mater. Lett.* **2003**, *57*, 3992−3997.

(13) Yu, K.; Kim, D. J.; Chung, H. S.; Liang, H. Dispersed Rodlike Nickel Powder Synthesized by Modified Polyol Process. *Mater. Lett.* **2003**, *57*, 3992−3997.

(14) Martin, C. R. Nanomaterials: A Membrane-Based Synthetic Approach. *Science* **1994**, *266*, 1961−1966.
(15) Martin, C. R. Membrane-Based Synthesis of Nanomaterials. *Chem. Mater.* **1996**, *8*, 1739−1746.
(16) Nielsch, K.; Muller, F.; Li, A.-P.; Gosele, U. Uniform Nickel Deposition into Ordered Alumina Pores by Pulsed Electrodeposition. *Adv. Mater.* **2000**, *12*, 582−586.
(17) Zhou, Z. F.; Zhou, Y. C.; Pan, Y.; Wang, X. G. Growth of the Nickel Nanorod Arrays Fabricated Using Electrochemical Deposition on Anodized Al Templates. *Mater. Lett.* **2008**, *62*, 3419−3421.
(18) Feiza, E.; Scott, K.; Baxendale, M.; Pal, C.; Ray, A. K.; Wang, W.; Pang, Y.; Hodgson, S. N. B. Synthesis and Characterisation of Nickel Nanorods for Cold Cathode Fluorescent Lamps. *Mater. Chem. Phys.* **2012**, *135*, 832−836.
(19) Bao, J.; Tie, C.; Xu, Z.; Zhou, Q.; Shen, D.; Ma, Q. Template Synthesis of an Array of Nickel Nanotubules and Its Magnetic Behavior. *Adv. Mater.* **2001**, *13*, 1631−1633.
(20) Narayanan, T. N.; Shaijumon, M. M.; Ajayan, P. M.; Anantharaman, M. R. Synthesis of High Coercivity Core−Shell Nanorods Based on Nickel and Cobalt and Their Magnetic Properties. *Nanoscale Res. Lett.* **2010**, *5*, 164−168.
(21) Sander, M. S.; Gao, H. Aligned Arrays of Nanotubes and Segmented Nanotubes on Substrates Fabricated by Electrodeposition onto Nanorods. *J. Am. Chem. Soc.* **2005**, *127*, 12158−12159.
(22) Evans, P.; Hendren, W. R.; Atkinson, R.; Wurtz, G. A.; Dickson, W.; Zayats, A. V.; Pollard, R. J. Growth and Properties of Gold and Nickel Nanorods in Thin Film Alumina. *Nanotechnology* **2006**, *17*, 5746−5753.
(23) Klein, T.; Laptev, A.; Gunther, A.; Bender, P.; Tschope, A.; Birringer, R. Magnetic-Field-Dependent Optical Transmission of Nickel Nanorod Colloidal Dispersions. *J. Appl. Phys.* **2009**, *106*, 114301−114306.
(24) Banerjee, A.; Halder, N. Electrochemical Growth of Ordered Nickel Nano-Rods Within a Composite Structure of Anodic-Alumina-Membrane/Metal/Silicon Substrate. *J. Nanosci. Nanotechnol.* **2010**, *10*, 4252−4258.
(25) Gunther, A.; Bender, P.; Tschope, A.; Birringer, R. Rotational Diffusion of Magnetic Nickel Nanorods in Colloidal Dispersions. *J. Phys.: Condens. Matter* **2011**, *23*, 1−14.
(26) Liu, C.-M.; Tseng, Y.-C.; Chen, C.; Hsu, M.-C.; Chao, T.-Y.; Cheng, Y.-T. Superparamagnetic and Ferromagnetic Ni Nanorod Arrays Fabricated on Si Substrates Using Electroless Deposition. *Nanotechnology* **2009**, *20*, 415703−415710.
(27) Mohl, M.; Kumar, A.; Reddy, A. L. M.; Kukovecz, A.; Konya, Z.; Kiricsi, I.; Vajtai, R.; Ajayan, P. M. Synthesis of Catalytic Porous Metallic Nanorods by Galvanic Exchange Reaction. *J. Phys. Chem. C* **2010**, *114*, 389−393.
(28) Nguyen, P. P.; Pearson, D. H.; Tonucci, R. J. Fabrication and Characterization of Uniform Metallic Nanostructures Using Nanochannel Glass. *J. Electrochem. Soc.* **1998**, *145*, 247−251.
(29) Li, J.; Moskovits, M.; Haslett, T. L. Nanoscale Electroless Metal Deposition in Aligned Carbon Nanotubes. *Chem. Mater.* **1998**, *10*, 1963−1967.
(30) Tyagi, P. K.; Misra, A.; Singh, M. K.; Misra, D. S.; Ghatak, J. High-Resolution Transmission Electron Microscopy Mapping of Nickel and Cobalt Single-Crystalline Nanorods Inside Multiwalled Carbon Nanotubes and Chirality Calculations. *Appl. Phys. Lett.* **2005**, *86*, 253110−1−253110−3.
(31) Kulshrestha, N.; Hazra, K. S.; Bajpai, R. R.; Mohapatra, D. R.; Misra, D. S. Structural Changes in Nickel Nanaorods Encapsulated in Carbon Nanotubes by 200 kV Electron Irradiation in TEM. *AIP Conf. Proc.* **2010**, *1313*, 259−261.
(32) He, Z.; Lee, C. S.; Maurice, J.-L.; Pribat, D.; Haghi-Ashtiani, P.; Cojocaru, C. S. Vertically Oriented Nickel Nanorod/Carbon Nanofiber Core/Shell Structures Synthesized by Plasma-Enhanced Chemical Vapor Deposition. *Carbon* **2011**, *49*, 4710−4718.
(33) Whitney, T. M.; Searson, P. C.; Jiang, J. S.; Chien, C. L. Fabrication and Magnetic Properties of Arrays of Metallic Nanowires. *Science* **1993**, *261*, 1316−1319.
(34) Xue, S.; Cao, C.; Zhu, H. Electrochemically and Template-Synthesized Nickel Nanorod Arrays and Nanotubes. *J. Mater. Sci.* **2006**, *41*, 5598−5601.
(35) Xue, S. H.; Wang, Z. D. Metal Nanorod Arrays and Their Magnetic Properties. *Mater. Sci. Eng., B* **2006**, *135*, 74−77.
(36) Sando, G. M.; Berry, A. D.; Owrutsky, J. C. Ultrafast Studies of Gold, Nickel, and Palladium Nanorods. *J. Chem. Phys.* **2007**, *127*, 074705−1−074705−11.
(37) Seifarth, O.; Krenek, R.; Tokarev, I.; Burkov, Y.; Sidorenko, A.; Minko, S.; Stamm, M.; Schmeiber, D. Metallic Nickel Nanorod Arrays Embedded Into Ordered Block Copolymer Templates. *Thin Solid Films* **2007**, *515*, 6652−6556.
(38) Jou, S.; Yeh, D.-Y.; Tseng, A. A. Nickel Nanorods Produced by Annealing Composite Oxide Films. *J. Nanosci. Nanotechnol.* **2008**, *8*, 390−392.
(39) Zhang, Z.; Dai, S.; Blom, D. A.; Shen, J. Synthesis of Ordered Metallic Nanowires Inside Ordered Mesoporous Materials Through Electroless Deposition. *Chem. Mater.* **2002**, *14*, 965−968.
(40) Li, H.; Lin, H.; Xie, S.; Dai, W.; Qiao, M.; Lu, Y.; Li, H. Ordered Mesoporous Ni Nanowires with Enhanced Hydrogenation Activity Prepared by Electroless Plating on Functionalized SBA-15. *Chem. Mater.* **2008**, *20*, 3936−3943.
(41) Zhang, Z.; Pan, Z.; Mahurin, S. M.; Dai, S. Synthesis of Ultrahigh-Density Ordered Arrays of Metallic Nickel Nanowires in Mesoporous Silica Films. *Chem. Commun.* **2003**, *20*, 2584−2585.
(42) Bae, C.; Yoo, H.; Kim, S.; Lee, K.; Kim, J.; Sung, M. M.; Shin, H. Template-Directed Synthesis of Oxide Nanotubes: Fabrication, Characterization, and Applications. *Chem. Mater.* **2008**, *20*, 756−767.
(43) Jung, J. H.; Park, M.; Shinkai, S. Fabrication of Silica Nanotubes by Using Self-Assembled Gels and Their Applications in Environmental and Biological Fields. *Chem. Soc. Rev.* **2010**, *39*, 4286−4302.
(44) Yang, X.; Tang, H.; Cao, K.; Song, H.; Sheng, W.; Wu, Q. Templated-Assisted One-Dimensional Silica Nanotubes: Synthesis and Applications. *J. Mater. Chem.* **2011**, *21*, 6122−6135.
(45) Nakamura, H.; Matsui, Y. Silica Gel Nanotubes Obtained by the Sol-Gel Method. *J. Am. Chem. Soc.* **1995**, *117*, 2651−2652.
(46) Ono, Y.; Nakashima, K.; Sano, M.; Kanekiyo, Y.; Inoue, K.; Hojo, J.; Shinkai, S. Organic Gels are Useful as a Template for the Preparation of Hollow Fiber Silica. *Chem. Commun.* **1998**, *14*, 1477−1478.
(47) Wang, L.; Tomura, S.; Ohashi, F.; Maeda, M.; Suzuki, M.; Inukai, K. Synthesis of Single Silica Nanotubes in the Presence of Citric Acid. *J. Mater. Chem.* **2001**, *11*, 1465−1468.
(48) Mitchell, D. T.; Lee, S. B.; Trofin, L.; Li, N.; Nevanen, T. K.; Soderlund, H.; Martin, C. R. Smart Nanotubes for Bioseparations and Biocatalysis. *J. Am. Chem. Soc.* **2002**, *124*, 11864−11865.
(49) Kovtyukhova, N. I.; Mallouk, T. E.; Mayer, T. S. Templated Surface Sol-Gel Synthesis of SiO_2 Nanotubes and SiO_2-Insulated Metal Nanowires. *Adv. Mater.* **2003**, *15*, 780−785.
(50) Jang, J.; Yoon, H. Novel Fabrication of Size-Tunable Silica Nanotubes Using a Reverse-Microemulsion-Mediated Sol-Gel Method. *Adv. Mater.* **2004**, *16*, 799−802.
(51) Kim, M.; Hong, J.; Lee, J.; Hong, C. K.; Shim, S. E. Fabrication of Silica Nanotubes Using Silica Coated Multi-Walled Carbon Nanotubes as the Template. *J. Colloid Interface Sci.* **2008**, *322*, 321−326.
(52) Yu, Y.; Qiu, H.; Wu, X.; Li, H.; Li, Y.; Sakamoto, Y.; Inoue, Y.; Sakamoto, K.; Terasaki, O.; Che, S. Synthesis and Characterization of Silica Nanotubes with Radially Oriented Mesopores. *Adv. Funct. Mater.* **2008**, *18*, 541−550.
(53) Yu, J.; Bai, X.; Suh, J.; Lee, S. B.; Son, S. J. Mechanical Capping of Silica Nanotubes for Encapsulation of Molecules. *J. Am. Chem. Soc.* **2009**, *131*, 15574−15575.
(54) Jiang, J.; Wang, T.; Liu, M. Creating Chirality in the Inner Walls of Silica Nanotubes through a Hydrogel Template: Chiral Transcription and Chiroptical Switch. *Chem. Commun.* **2010**, *46*, 7178−7180.

(55) Chen, X.; Berger, A.; Ge, M.; Hopfe, S.; Dai, N.; Gosele, U.; Schlecht, S.; Steinhart, M. Silica Nanotubes by Templated Thermolysis of Silicon Tetraacetate. *Chem. Mater.* **2011**, *23*, 3129−3131.
(56) Zhang, A.; Hou, K.; Gu, L.; Dai, C.; Liu, M.; Song, C.; Guo, X. Synthesis of Silica Nanotubes with Orientation Controlled Mesopores in Porous Membranes via Interfacial Growth. *Chem. Mater.* **2012**, *24*, 1005−1010.
(57) Adachi, M.; Harada, T.; Harada, M. Formation of Huge Length Silica Nanotubes by a Templating Mechanism in the Laurylamine/Tetraethoxysilane System. *Langmuir* **1999**, *15*, 7097−7100.
(58) Numata, M.; Sugiyasu, K.; Hasegawa, T.; Shinkai, S. Sol−Gel Reaction Using DNA as a Template: An Attempt Toward Transcription of DNA into Inorganic Materials. *Angew. Chem., Int. Ed.* **2004**, *43*, 3279−3283.
(59) Ding, S.; Liu, N.; Li, X.; Peng, L.; Guo, X.; Ding, W. Silica Nanotubes and Their Assembly Assisted by Boric Acid to Hierachical Mesostructures. *Langmuir* **2010**, *26*, 4572−4575.
(60) Zhang, M.; Zhang, W.; Wang, S. Synthesis of Well-Defined Silica and Pd/Silica Nanotubes through a Surface Sol-Gel Process on a Self-Assembled Chelate Block Copolymer. *J. Phys. Chem. C* **2010**, *114*, 15640−15644.
(61) Zhang, Y.; Son, S. J. Fluorescent Magnetic Silica Nanotubes with High Photostability Prepared by the Conventional Reverse Micro-Emulsion Method. *Bull. Korean Chem. Soc.* **2012**, *33*, 4165−4168.
(62) Song, M.-M.; Bi, H.; Zhang, Y. Fabrication of Fe@mSiO_2 Nanowires with Large Remanence and Low Cytotoxicity for Targeted Drug Delivery. *J. Appl. Phys.* **2012**, *111*, 07B302−1−07B302−3.
(63) Zhou, H.; Chen, J.; Sutter, E.; Feygenson, M.; Aronson, M. C.; Wong, S. S. Water-Dispersible, Multifunctional, Magnetic, Luminescent Silica-Encapsulated Composite Nanotubes. *Small* **2010**, *6*, 412−420.
(64) Dahlberg, K. A.; Schwank, J. W. Synthesis of Ni@SiO_2 Nanotube Particles in a Water-in-Oil Microemulsion Template. *Chem. Mater.* **2012**, *24*, 2635−2644.
(65) Takenaka, S.; Umebayashi, H.; Tanabe, E.; Matsune, H.; Kishida, M. Specific Performance of Silica-Coated Ni Catalysts for the Partial Oxidation of Methane to Synthesis Gas. *J. Catal.* **2007**, *245*, 392−400.
(66) Tu, C.; Du, J.; Yao, L.; Yang, C.; Ge, M.; Xu, C.; Gao, M. Magnetic Ni/SiO_2 Composite Microcapsules Prepared by "One-Pot" Synthesis. *J. Mater. Chem.* **2008**, *19*, 1245−1251.
(67) Park, J. C.; Bang, J. U.; Lee, J.; Ko, C. H.; Song, H. Ni@SiO_2 Yolk-Shell Nanoreactor Catalysts: High Temperature Stability and Recyclability. *J. Mater. Chem.* **2009**, *20*, 1239−1246.
(68) Gao, C.; Lu, Z.; Yin, Y. Gram-Scale Synthesis of Silica Nanotubes with Controlled Aspect Ratios by Templating of Nickel-Hydrazine Complex Nanorods. *Langmuir* **2011**, *27*, 12201−12208.
(69) Park, J. W.; Chae, E. H.; Kim, S. H.; Ho Lee, J.; Kim, J. W.; Mi Yoon, S.; Choi, J. Preparation of Fine Ni Powders from Nickel Hydrazine Complex. *Mater. Chem. Phys.* **2006**, *97*, 371−378.
(70) Nicholls, D.; Swindells, R. Hydrazine Complexes of Nickel(II) Chloride. *J. Inorg. Nucl. Chem.* **1968**, *30*, 2211−2217.
(71) Sacconi, L.; Sabantini, A. The Infra-Red Spectra of Metal(II)-Hydrazine Complexes. *J. Inorg. Nuclear Chem.* **1963**, *25*, 1389−1393.
(72) Nicholls, D.; Rowley, M.; Swindells, R. Hydrazine Complexes of Cobalt(II) Chloride. *J. Chem. Soc. A* **1966**, 950−952.
(73) Bruynooghe, S.; Bertin, F.; Chabli, A.; Gay, J.-C.; Blanchard, B.; Couchaud, M. Infrared Spectroscopic Ellipsometry for Residual Water Detection in Annealed Sol-Gel Thin Layers. *Thin Solid Films* **1998**, *313*−*314*, 722−726.
(74) Patil, K. C. Metal-Hydrazine Complexes as Precursors to Oxide Materials. *Proc. Indian Acad. Sci. (Chem. Sci.)* **1986**, *96*, 459−464.
(75) Chen, X.; Zhang, T.; Zheng, M.; Wu, Z.; Wu, W.; Li, C. The Reaction Route and Active Site of Catalytic Decomposition of Hydrazine over Molybdenum Nitride Catalyst. *J. Catal.* **2004**, *224*, 473−478.
(76) Lif, J.; Skoglundh, M.; Löwendahl, L. Sintering of Nickel Particles Supported on Alumina in Ammonia. *Appl. Catal., A* **2002**, *228*, 145−154.
(77) Wu, Z.; Ge, S.; Zhang, M.; Li, W.; Mu, S.; Tao, K. Controlled Synthesis of Supported Nickel Boride Catalyst Using Electroless Plating. *J. Phys. Chem. C* **2007**, *111*, 8587−8593.
(78) Deng, J.; Li, H.; Wang, W. Progress in Design of New Amorphous Alloy Catalysts. *Catal. Today* **1999**, *51*, 113−125.
(79) Lee, S.; Chen, Y. Selective Hydrogenation of Furfural on Ni-P, Ni-B, and Ni-P-B Ultrafine Materials. *Ind. Eng. Chem. Res.* **1999**, *38*, 2548−2556.
(80) Mallory, G. O.; Hajdu, J. B. The Fundamental Aspects of Electroless Nickel Plating. In *Electroless Plating: Fundamentals and Applications*; American Electroplaters and Surface Finishers Society: Orlando, FL, 1990, Chapter 1, p 14.
(81) Li, H.; Li, H.; Deng, J. The Crystallization Process of Ultrafine Ni−B Amorphous Alloy. *Mater. Lett.* **2001**, *50*, 41−46.
(82) Mueller, R.; Kammler, H. K.; Wegner, K.; Pratsinis, S. E. OH Surface Density of SiO_2 and TiO_2 by Thermogravimetric Analysis. *Langmuir* **2003**, *19*, 160−165.
(83) Son, S. J.; Reichel, J.; He, B.; Schuchman, M.; Lee, S. B. Magnetic Nanotubes for Magnetic-Field-Assisted Bioseparation, Biointeraction, and Drug Delivery. *J. Am. Chem. Soc.* **2005**, *127*, 7316−7317.
(84) Boudjahem, A. G.; Monteverdi, S.; Mercy, M.; Bettahar, M. M. Study of Nickel Catalysts Supported on Silica of Low Surface Area and Prepared by Reduction of Nickel Acetate in Aqueous Hydrazine. *J. Catal.* **2004**, *221*, 325−334.
(85) Bartholomew, C. H. Sintering and Redispersion of supported Metals: Perspectives from the Literature of the Past Decade. In *Catalyst Deactivation 1997*; Bartholomew, C. H., Fuentes, G. A., Eds.; Studies in Surface Science and Catalysis; Elsevier Science: Amsterdam, The Netherlands, 1997; Vol. *111*, pp 585−592.
(86) Nakayama, T.; Arai, M.; Nishiyama, Y. Dispersion of Nickel Particles Supported on Alumina and Silica in Oxygen and Hydrogen. *J. Catal.* **1984**, *87*, 108−115.
(87) Arai, M.; Ishikawa, T.; Nishiyama, Y. Surface Migration of Ni on C, SiO_2, and Al_2O_3. *J. Phys. Chem.* **1982**, *86*, 577−581.
(88) Larson, A. C.; Von Dreele, R. B. General Structure Analysis System, Los Alamos National Laboratory Report LAUR 86-748, 2000.
(89) Legrand, J.; Taleb, A.; Gota, S.; Guittet, M.-J.; Petit, C. Synthesis and XPS Characterization of Nickel Boride Nanoparticles. *Langmuir* **2002**, *18*, 4131−4137.
(90) Lu, K.; Zhu, X. Nickel−Boron Nanolayer Evolution on Boron Carbide Particle Surfaces during Thermal Treatment. *Thin Solid Films* **2009**, *517*, 4479−4483.
(91) Berger, S. V. The Crystal Structure of Boron Oxide. *Acta Chem. Scand.* **1953**, *7*, 611−622.
(92) Li, H.; Xu, Y. Liquid Phase Benzene Hydrogenation to Cyclohexane over Modified Ni−P Amorphous Catalysts. *Mater. Lett.* **2001**, *51*, 101−107.
(93) Li, H.; Lin, H.; Xie, S.; Dai, W.; Qiao, M.; Lu, Y.; Li, H. Ordered Mesoporous Ni Nanowires with Enhanced Hydrogenation Activity Prepared by Electroless Plating on Functionalized SBA-15. *Chem. Mater.* **2008**, *20*, 3936−3943.